ELSEVIER

Contents lists available at ScienceDirect

Desalination

journal homepage: www.elsevier.com/locate/desal





Multipass hollow fiber membrane modules for membrane distillation

Jheng-Han Tsai ^a, Cejna Quist-Jensen ^b, Aamer Ali ^{b,*}

- ^a Department of Chemical Engineering and Biotechnology, Philippa Fawcett Drive, Cambridge CB3 OAS, UK
- b Department of Chemistry and Bioscience, Aalborg University, Fredrik Bajers Vej 7H, 9220 Aalborg, Denmark

HIGHLIGHTS

- New multipass module designs for membrane distillation are proposed
- Thermal energy consumption of the proposed modules is studied as function of module design parameters and flow arrangement
- The proposed designs demonstrate up to 35 % less thermal energy consumption than the conventional single pass design
- The proposed designs exhibit productivity several times higher than the traditional single-pass design

ARTICLE INFO

Keywords: Membrane distillation Energy efficiency Hollow fibers Multipass modules

ABSTRACT

Membrane distillation (MD) is an interesting process for desalination; however high thermal energy consumption remains one of the main obstacles in its widespread adoption. The current study presents multipass hollow fiber membrane modules to improve thermal efficiency of MD process. Fundamentally three module designs are considered: conventional one shell and one tube (fiber) pass (A), 1 shell and multiple tube passes (B/C) and equal but multiple shell and tube passes (D). The performance of the proposed designs is analyzed as a function of length of each pass, number of passes and operating conditions by using Aspen Plus simulator. The results demonstrate that the traditional design A yields the highest flux — up to 92 % higher than the multipass design D. On the other hand, the multipass design D is the most energy efficiency and shows up to 35 % less thermal energy consumption than the conventional single pass design of the same length. Single shell and multiple tube pass designs (B/C) show higher flux than D; however, their specific thermal energy consumption remains the highest among all the designs investigated. The pressure drop in multipass modules was marginally (1.5 %) higher than the conventional single pass modules.

1. Introduction

Membrane distillation (MD) has gained significant interest for desalination and related applications [1]. The process operates with thermal energy supplied to generate vapor from a solution which is in contact with a microporous hydrophobic membrane. The vapor pass through the membrane pores while the solution, along with the non-volatiles, is retained by the hydrophobic membrane. MD has been extensively researched during the last two decades for the development of appropriate membranes [2–4], process understanding and improvement [3,5–9], new applications [10–13] and novel schemes and strategies to improve the energy efficiency of the process [14–19]. Flat sheet membranes have been dominating the pilot and commercial-sale applications of MD; however, hollow fibers are gaining significant

attention due to their self-supporting structure, high packing density, and large membrane surface area [20].

Despite promising studies carried out at lab and pilot-scale, high thermal energy demand of MD remains the bottleneck in widespread commercial adoption of the process [21,22]. This is particularly applicable for the direct contact MD (DCMD) which is the simplest configuration of MD but suffers from high thermal conductive losses due to the direct contact of feed and permeate streams with opposite sides of the membrane. A proven solution to decrease the net thermal energy consumption of MD is to recover the latent heat of condensation as sensible heat to preheat the feed in multi-stage arrangements [23–25]. In this context, the length over which feed and permeate streams stay in contact with the membrane plays an important role i.e., long the length, higher the temperature of the permeate stream that can be eventually used to

E-mail address: aa@bio.aau.dk (A. Ali).

 $^{^{\}ast}$ Corresponding author.

transfer heat to the feed stream [26]. Long contact lengths also use thermal energy of feed more efficiently that eventually contributes to lowering the energy consumption of the process [27,28]. This aspect has been highlighted in some of the recent publications on module designs for large-scale MD applications. Winter et al. studied the effect of channel length of DCMD modules on the gain to output ratio (GOR), a measure of how much freshwater is produced by the latent heat of 1 kg of heating steam [29]. The authors noted that GOR can be increased up to 3 times by increasing the flow channel length from 1 to 7 m. Ruiz-Aguirre et al. also reported the similar observations: the specific thermal energy consumption (STEC) of MD decreased from 296 to 107 kWh/ m³ by increasing the channel length from 1.5 to 5 m [30]. Ali et al. demonstrated that the STEC of DCMD can be reduced up to 23 % by increasing the channel (module) length from 1 to 10 m [31]. In a study performed on air gap MD, STEC reduced from 374 to 200 kWh/m³ by increasing the channel length from 3.5 to 10 m [28].

The conventional hollow fiber membrane module for MD is a shell and tube arrangement where hot feed and cold permeate streams, generally flowing in countercurrent mode, exit the module after completing one pass. An optimum channel length for hollow fiber membrane modules for MD is dependent upon the process and membrane parameters and our previous studies demonstrate that its value can exceed several meters [31-34]. However, currently there are no hollow module designs available to accommodate long module lengths. Manufacturing of long hollow fiber membrane modules is challenging due to certain design and manufacturing-related constraints. In long modules, fibers can touch each other to reduce the effective membrane area [35] and entire surface of the fiber may not be exposed to the shell side fluid in case of direct contact membrane distillation [36]. The hydrodynamics in long modules are also difficult to maintain at the desired uniform level, particularly at shell side [36]. Additionally, the long fiber lengths may not be suitable for the situations where the available space is limited. Due to these constraints, commercial hollow fiber membrane modules are generally around 1 m in length [38,39]. Thus, the conventional single-pass hollow fiber membrane module design for MD is not suitable to accommodate long fiber lengths which limits the energy efficiency of the existing designs. Connecting multiple modules in series is the current norm to achieve large effective module length; however, it increases physical footprints of the process, decreases productivity per module, and may cause additional issues such as leakage from the connections [40].

To address the aforementioned issues, the relevant solutions from process industry can be adopted. For heat exchangers, multipass designs have been suggested to achieve various heating/cooling requirements [41,42]. Multiple passes can be incorporated on shell as well as on tubes side. After completing one pass, the fluid reverses its direction within the heat exchanger. In case of tubes, the fluid leaves the tubes after completing each pass and is reintroduced into the tubes to commence the next pass. To reverse the fluid direction on shell side, a longitudinal baffle is introduced into the shell so that the fluid flows above and below the baffle during the consecutive passes. Such designs are a proven solution in process industry to reduce the overall length of heat exchangers by several times [42–44].

Inspired from the concept of multi-pass heat exchangers, the current study investigates innovative multipass hollow fiber membrane modules for DCMD. Unlike the traditional single pass design, the proposed designs allow packing long fibers within a given module length that results into lower STEC of the process and improved productivity. The study has been performed by considering single shell and multiple tube passes as well as multiple shell and tube passes (maximum 8 at each side). In a single shell and multiple fiber passes configuration, the effect of varying the fluid arrangement (1st or 2nd pass in cocurrent) has also been investigated. The initial analysis has been conducted for the two-pass (on fiber and/or shell sides) modules by considering relatively long (2.5–5 m) pass lengths. Later in the manuscript, the analysis has been extended to study the modules performance, in terms of STEC, as a

function of number of passes on shell and fiber side, length of each pass and operating conditions including feed temperature and the ratio of feed to the permeate flow rate (F/P).

2. Materials and methods

2.1. Module configurations considered

Different MD module designs, like the multipass heat exchangers, have been considered. The first design configuration (A) is a conventional hollow fiber membrane module (Fig. 1 (a) and Fig. A1 (a) in the Appendix) where the permeate and feed flow in the module in countercurrent directions and exit the module hereafter. The second design configuration (Fig. 1 (b) and (c)) represents 2-1 arrangement where the fluid introduced inside the fiber flows in half of the fibers during 1st pass and changes its direction before flowing into the other half of the fibers during the 2nd pass. The direction can be changed by looping back the fibers as suggested in literature [45] or by introducing the cover cap as applied for heat exchanger applications [42,46]. The fluid in the shell flows only once in this configuration. The fluid inside the fibers can have either 1st pass as cocurrent and the 2nd pass as countercurrent to the permeate (Fig. 1 (b)) or the other way around (Fig. 1 (c)). In this study, these designs are named as designs B and C, respectively. In the last design (D), both feed and permeate streams have two passes in pure countercurrent configuration (Fig. 1 (d)). For the configurations shown in Fig. 1 (b)-(d), the number of passes can be extended to any value; however, in practical applications, the number will be restricted due to the corresponding pressure drop associated with long flow lengths [34]. In this study, the maximum 8 number of passes with the maximum pass length of 2.5 m have been analyzed. The feed temperature has been varied from 50 to 80 °C and the effect of F/P ratio has been investigated by changing the ratio from 1 to 7.

For the initial analysis (Section 3.1) of temperature profiles and overall flux, the length of each pass has been fixed at 2.5 m and the feed with an inlet temperature of 80 °C and inlet velocity of 0.1 m/s has been introduced. Permeate inlet temperature and velocity were kept constant at 25 °C and 0.1 m/s, respectively, for all the configurations. Thus, to keep the feed inlet velocity (V_f) same in all the module configurations, the membrane area is the lowest for configuration A with respect to the other configurations due to only one pass involved in this configuration. In the configurations B, C and D, the membrane area in each pass is equal to that for the configuration A i.e., the total membrane area (or number of fibers) in each of these configurations is twice compared to the configuration A. It implies that, for the same packing density in all the configurations, shell side cross flow area for the permeate stream will be double in the configuration B and C. Thus, to keep the permeate inlet velocity equal to that in configuration (A), the proportionally high permeate flow rate must be introduced in the configurations B and C.

Theoretical and experimental investigations for the model validation (see Appendix) are carried out by using PP hollow fiber membrane purchased from Membrana GmbH. Overall porosity (ϵ), average pore size (r) and thickness (δ) of the membrane are 73 %, 0.2 μ m and 450 μ m, respectively.

2.2. Model development

The details about the model development have been described elsewhere [33]. The procedure has been explained briefly here. Equations describing heat transfer in MD can be written as:

$$J_{H} = H\left(T_{fm} - T_{pm}\right) = J_{M}\Delta h_{v} + \frac{k_{m}}{\delta}\left(T_{fm} - T_{pm}\right) \tag{1}$$

Here J_H is the heat flux $(J/(m^2 \cdot s))$, H is the overall heat transfer coefficient $(W/m^2 \cdot K)$, T_{fm} and T_{pm} are the membrane surface temperatures (K) on feed and permeate sides, respectively, Δh_V is the latent heat (J/kg) of water vapor, k_m is thermal conductivity $(W/m \cdot K)$ of the

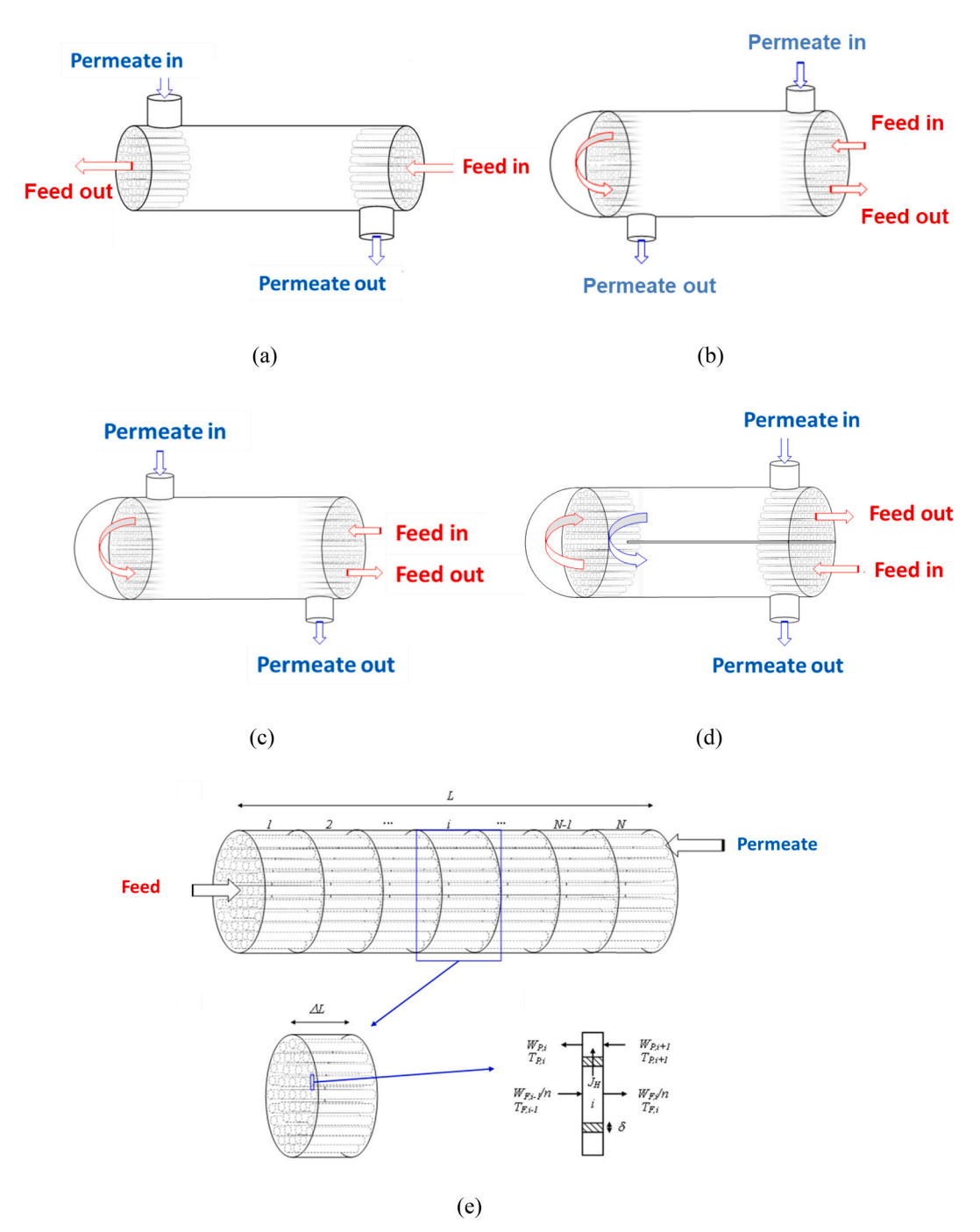


Fig. 1. Various module designs considered in the current study. (a) traditional single pass configurations where feed and permeate flow in pure countercurrent (b) two feed pass configuration where first pass is in cocurrent with the permeate and 2nd one is in countercurrent (c) two feed pass configuration where first pass is in countercurrent with the permeate and 2nd one is in cocurrent (d) feed and permeate are in countercurrent in two passes (e) schematic of membrane module and heat and mass transfer in an element from the module used in the modeling.

membrane and has been calculated using the following correlation $\[2\]$:

$$k_m = k_p(1 - \varepsilon) + k_g \varepsilon \tag{2}$$

where $k_{\rm p}$ and $k_{\rm g}$ represent the thermal conductivities of polymer and gas (air) inside the pores, respectively.

Mass transfer flux across the membrane can be written as:

$$J_M = C(P_{fm} - P_{pm}) \tag{3}$$

where C is the vapor permeability coefficient of the membrane, P_{fm} and P_{pm} (Pa) denote the vapor pressures at the membrane surfaces at the feed

and permeate sides, respectively and can be calculated by using the Antoine equation as following:

$$P_{m,f/p} = exp\left(23.1964 - \frac{3816.44}{T_{m,F/P} - 46.13}\right) \tag{4}$$

The average pore size of the membrane considered in current study is close to the mean free path of water vapor ($\sim\!0.11~\mu m$ [47]), therefore, combined Knudsen-molecular diffusion model has been considered in the current study to calculate C.

$$C = \left[\frac{3\tau\delta}{2\varepsilon r} \left(\frac{\pi RT}{8M} \right)^{1/2} + \frac{r\delta P_a RT}{\varepsilon PDM} \right]^{-1}$$
 (5)

where τ is the membrane tortuosity factor, R is the universal gas constant (J/K·mol), T is the temperature (K) inside the membrane which is taken equal to the average of the temperature at the membrane surfaces, M is the molecular weight of water (kg/mol), P_a is the air pressure in the membrane (Pa), P is the total pressure inside the pore (Pa), and D is the diffusion coefficient of water vapor (m²/s). Pa was taken equal to the atmospheric pressure and the diffusivity (product of P and D) of water vapor through the air present inside the pores was calculated according to the following correlation [48]:

$$PD = 1.895 \times 10^{-5} T^{2.072} \tag{6}$$

 τ was calculated by using the ε according to the following correlation [49]:

$$\tau = \frac{(2 - \varepsilon)^2}{\varepsilon} \tag{7}$$

In DCMD, two liquid streams with different temperatures are in contact with two opposite sides of membrane therefore, due to the heat transfer through conduction and convection, the temperature of feed stream at the membrane surface is less than its corresponding value in the bulk while permeate at membrane surface has higher temperature than its corresponding value in bulk. Heat transfer within the two channels can be described as following:

$$J_H = h_f \left(T_f - T_{fm} \right) \tag{8}$$

$$J_{H,p} = h_p \left(T_{pm} - T_p \right) \tag{9}$$

here $h_{\rm F}$ and $h_{\rm P}$ (W/m²·K) are the film heat transfer coefficients of the feed and permeate sides, respectively, whereas $T_{\rm F}$ and $T_{\rm P}$ are the bulk temperatures of the feed and permeate streams, respectively. $h_{\rm F}$ and $h_{\rm P}$ are essential to determine the temperatures at the membrane surfaces.

For the type of membrane and module considered in this study, the following correlations were found to be the most suitable to calculate the Nusselt number and, thereupon, the corresponding heat transfer coefficients [19,26]. These were therefore used in the study.

Lumen side:

$$Nu = 3.66 + \frac{0.19Gz^{0.8}}{1 + 0.117Gz^{0.467}} \left(\frac{\mu}{\mu_W}\right)^{0.14}$$
 (10)

Shell side:

$$Nu = 0.16Re^{0.6}Pr^{0.33} \left(\frac{\mu}{\mu_W}\right)^{0.14} \tag{11}$$

where Nu , Gz , Re and Pr are Nusselt number, Graetz number, Reynolds number and Prandtl number, respectively.

Heat transfer coefficient is linked with the Nu and channel diameter D_c (m) as following:

$$h_{p/f} = \frac{Nu_{f/p}.K}{D_c} \tag{12}$$

where K is thermal conductivity of the fluid inside the channel.

Temperatures at the membrane surface on feed and permeate sides can be calculated by using the operating temperatures and different heat transfer coefficients as following:

$$T_{fm} = T_f - \left(T_f - T_p\right) \frac{\frac{1}{h_f}}{\frac{1}{h_v + h_m} + \frac{1}{h_f} + \frac{1}{h_p}} \tag{13}$$

$$T_{pm} = T_p + \left(T_f - T_p\right) \frac{1}{\frac{1}{h_b + h_m} + \frac{1}{h_c} + \frac{1}{h_c}} \tag{14}$$

where h_m and h_v are the heat transfer coefficients of membrane and vapor, respectively.

Temperature profiles along the modules were calculated by performing the energy balance on two consecutive elements along the module that can be expressed with the following equation:

$$(n\pi D_{in}\Delta L)J_{H} = \begin{cases} W_{F}C_{P,F} \left[T_{F}^{(i-1)} - T_{F}^{(i)} \right] \\ W_{P}C_{P,P} \left[T_{P}^{(i)} - T_{P}^{(i+1)} \right] \end{cases}$$
(15)

where W_F and W_P are the mass flow rates (kg/s) of the feed and permeate streams, respectively, whereas $C_{P, F}$ and $C_{P, P}$ are the heat capacities (J/kg·K) of the feed and permeate, respectively.

STEC in kWh/m^3 is calculated by using the following expression:

$$STEC = \frac{W_F C_{P,F} (T_{fin} - T_{fo})}{3600 J_M A}$$
 (16)

where *A* is the total membrane area.

In cases where the permeate outlet temperature exceeds the feed outlet temperature by >5 °C, the heat recovery from the permeate stream was accomplished by partly heating the feed stream before reintroducing into the module. Thus, in these cases, the net STEC was calculated by subtracting the recovered heat from the externally supplied heat input calculated through Eq. (16).

The flowsheet simulation was developed using the commercial software Aspen Plus V8.8. The physicochemical properties for water were correlated by the "ELEC-NRTL" model. The schematic of module and an element from the module taken for the analysis has been shown in Fig. A1 [33]. The simulation of the MD module was developed using the Aspen user customized unit model based on the model demonstrated above. In all cases, the Fast Newton method was chosen to calculate models due to its short calculation time. For estimation and optimization, the Hypsqp optimizer was adopted, which is a feasible path successive quadratic programming optimizer. It ensures that all upper and lower bounds on the decision, and variables are never violated.

In addition to the heat and mass transport, pressure drop within the module is an important parameter that does not only determine the electric energy consumption related with circulation of the fluid but also affects the non-wettability behavior of the membrane pores. To fulfil the non-wettability condition, the pressure drop within the membrane module should be less than the liquid entry pressure of the membrane pores. Therefore, the pressure drop associated with the overall fiber length, reversal of flow direction at end of each pass and shell side of the module was analyzed. The following equation was used to calculate the pressure drop inside the overall fiber length L:

$$\Delta P_f = f \frac{L}{D_{in}} \frac{\rho v_f^2}{2} \tag{17}$$

where f, ρ , V_f and D_{in} represent the friction factor, density of the fluid (kg/m³), fluid velocity (m/s) and inner diameter of the membrane (m), respectively. The change of direction of the fluid after completing one pass introduced additional pressure drop known as return loss which was calculated according to the following correlation [43]:

$$\Delta P_r = 6\,894.8 \frac{4n}{s} \frac{v_f^2}{2g} \tag{18}$$

where n, s and g represent total number of passes, specific gravity of the feed solution and acceleration of gravity (m/ s^2), respectively.

To calculate the pressure drop on shell side of the module, the model proposed by Yoshikawa et al. was used [51]:

$$\Delta P_s = \frac{2k\mu}{\pi \varepsilon_s r_p^2 D_s^2} Q_s \tag{19}$$

 μ , ε_s , r_{lv} , D_s and Q_s in the above equation represent dynamic viscosity (Pa·s), void fraction, hydraulic radius (m), shell inside diameter (m) and flow rate (m³/s) inside the shell, respectively.

3. Results and discussion

3.1. Temperature profiles for the considered module designs

Bulk and membrane surface temperature profiles predicted by the validated model (see the details about validation in Appendix) for both feed and permeate streams for the considered module designs have been shown in Fig. 2. For the design A, it is evident from Fig. 2 (a) that the bulk as well as membrane surface temperature of the feed solution decreases almost linearly along the module and drops down to 62 °C from its initial value of 80 °C. The temperature of the permeate stream, on the other hand, increases from 25 to 52 $^{\circ}\text{C}$ at the exit of the module. The difference between the feed and permeate temperatures for the configuration A changes slightly along the module which is a characteristic of pure countercurrent mode. The configurations B and C demonstrate similar net temperature changes on the feed and permeate streams. For both the configurations, the final feed and permeate outlet temperature remained around 55 and 48 °C, respectively. For cocurrent passes (1st and 2nd pass in configurations B and C, respectively) of both the configurations, the temperature difference between the feed and permeate narrows down rapidly compared to the countercurrent passes. For instance, in case of the configuration B, the temperature difference decreases rapidly during the first (cocurrent) pass and increases again during the second pass ($T_{\rm fm}$ - $T_{\rm pm}$ equal to 12 and 23 °C, respectively). For the configuration C, where the feed and permeate are in countercurrent in 1st pass and in cocurrent during the second pass, the difference between the feed and permeate temperature is higher during the first pass compared to the second one. For the configuration D, the feed and permeate are in countercurrent in both the passes i.e. the 1st and 2nd

pass of feed are in countercurrent with the 2nd and 1st pass of permeate, respectively. Thus, the total contact length of the two streams in the configuration D is double of the configuration A which results into significantly higher outlet temperature of the permeate (i.e. 65 $^{\circ}\text{C}$) exceeding the feed outlet temperature of 56 $^{\circ}\text{C}$.

Fig. 2 also indicates that the temperature polarization (difference between the bulk and membrane surface temperature for feed or permeate) on feed and permeate sides is higher for those designs passes where feed and permeate are in cocurrent (Fig. 2 (b) and (c) for the designs B and C, respectively). This can be directly attributed to the higher initial trans-membrane temperature differences for cocurrent mode, as discussed in above paragraph, that induces higher driving force to conductive and convective heat transport across the membrane. In the configuration D, where the feed and permeate streams are in perfect countercurrent and difference between the feed and permeate streams is small, the temperature polarization is relatively modest.

3.2. Effect of pass length on the performance of two-pass module designs

F/P ratio is an important operating parameter that influences the MD performance and energy recovery potential and therefore, has been given special attention in this analysis. To investigate the effect of pass length on the process performance; flux, productivity, and STEC as functions of pass length at different F/P ratios have been plotted for all the considered designs in Fig. 3 (a)-(l). It is evident from Fig. 3 (a), (d), (g) and (j) that the flux is the highest for the shortest lengths and the lowest F/P considered for all the configurations. Short pass lengths provide high driving force whereas, under the comparable feed and permeate flow rates (corresponding to F/P ratios close to unity), the system is not limited by the mass transfer on feed or permeate side which ensures high driving force and contributes to the observed high flux [52]. As evident from Fig. 3 (b), (e), (h), and (k), the productivity (product of membrane area and the corresponding flux, denominator in Eq. (16)) is high for long pass lengths and low F/P ratios — the conditions that result into large membrane area and high flux, respectively. It

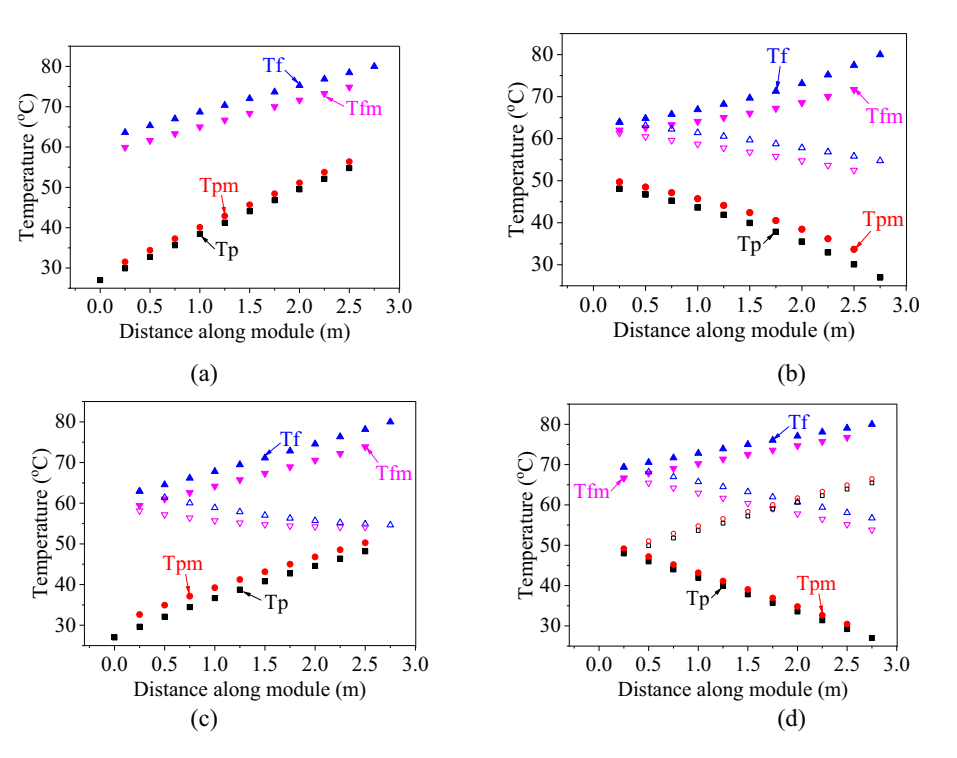


Fig. 2. Temperature profiles along module length at 80 °C and F/P = 2 for configuration (a) A (b) B (c) C, and (d) D. Subscripts f, p, fm and pm represent bulk feed temperature, bulk permeate temperature, temperature at the membrane surface on feed side and temperature at the membrane surface on permeate side, respectively.

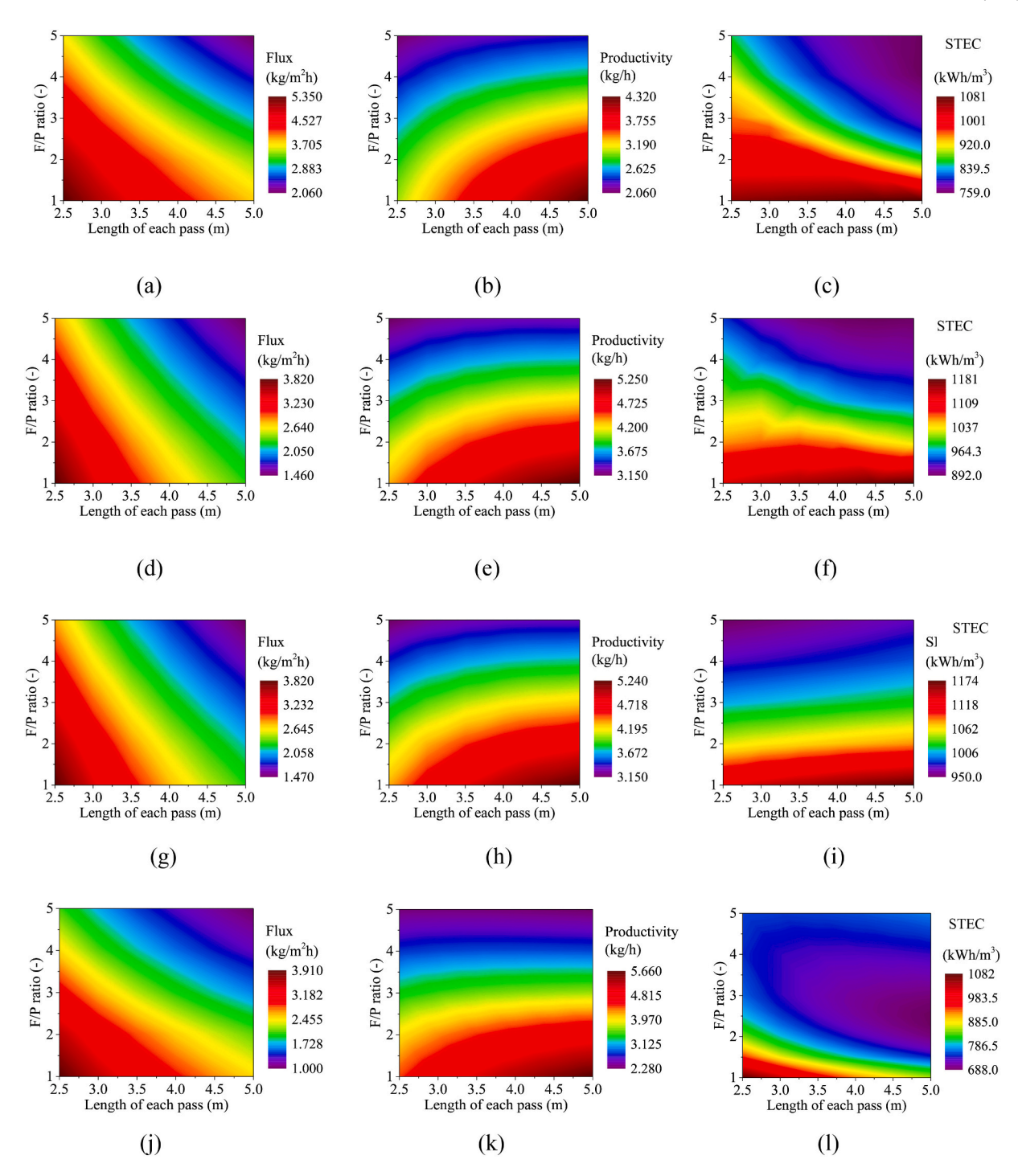


Fig. 3. Flux, productivity, and STEC as functions of length of modules and F/P ratio in (a)(b)(c) countercurrent (configuration A), (d)(e)(f) 1st pass in concurrent (configuration B), (g)(h)(i) 2nd pass in concurrent (configuration C), and (j)(k)(l) countercurrent in two zones (configuration D) at 80 °C, respectively.

is also interesting to note that the multipass configurations exhibit higher (up to 24 %) productivity than the traditional single pass configuration due to their ability to pack more membrane area within a module of given length.

The corresponding STEC for the considered configurations has been illustrated in Fig. 3 (c), (f), (i), and (l). It can be noticed from the figures that STEC responds differently to pass length and F/P ratio for the various configurations. In case of pure countercurrent configurations (A and D), STEC decreases by increasing the pass length (Fig. 3 (c) and (l)). Relatively higher decrease is observed for the configuration D where the STEC can be decreased by $\sim\!36$ % from its highest value (observed at the

shortest pass length and the lowest F/P ratio considered) by switching to the highest pass length and an appropriate F/P ratio. The observed decrease is expected as high pass length increases the module productivity and contact time of the two streams. The latter results into high permeate outlet temperature and low feed outlet temperature which is an indicator of efficient utilization of thermal energy and allows energy recovery from the permeate stream as explained elsewhere [31,33]. When the feed and permeate streams have comparable flow rates, utilization of the thermal energy of the feed is not efficient which restricts the heat recovery from the permeate stream as the outlet temperature of permeate does not exceed the feed outlet temperature which results into

high STEC as noted in Fig. 3 (c) and (l). It is also interesting to note that the minimum STEC for the configurations A and D appears at different F/P ratios. For the configuration A, the contact time of feed and permeate streams is half compared to the configuration D due to the corresponding difference in the effective length. Heat recovery for the configuration A will thus be possible (i.e. $T_{\rm pout} > T_{\rm fout} + 5$ °C) for high F/ P ratios i.e. under the conditions which promote sufficient heating of the permeate stream to make it suitable for heat recovery. On the other hand, the heat recovery condition can be met at a relatively low F/P ratio for the configuration D due to the long contact time of feed and permeate streams and therefore, the minimum STEC shifts at low F/P ratio (\sim 2.5). By further increasing the F/P ratio beyond this value, the flux decreases as the permeate temperature starts approaching the feed temperature; however, the energy recovery does not increase proportionally as explained elsewhere [33,34] and consequently, STEC starts increasing. Although the configuration D demonstrates the minimum flux, yet it also exhibits the lowest STEC due to better energy recovery achieved in this configuration. The minimum STEC observed for the configuration D is ~9 % lower than that for the configuration A, indicating superior energy efficiency of the configuration D.

For the configuration B and C (Fig. 3 (f) and (i)), the pass length affects STEC relatively less and both configurations show similar STEC which is significantly higher than the configurations A and D. Importantly, the minimum STEC (890 kWh/m³) for the configuration B appears at the long pass lengths and high F/P ratios. The configuration C exhibits the minimum STEC (950 kWh/m³) zone at short pass lengths and high F/P ratios. In case of the configuration B, the minimum STEC is observed under the conditions where the maximum energy recovery is possible — high pass-length and high F/P ratio. In contrast, it is clear that an optimum solution can be observed for the configuration D (Fig. 3 (l)), where the most appropriate design corresponds to the long pass lengths with an F/P ratio of $\sim\!2.5$.

3.3. Multipass module designs

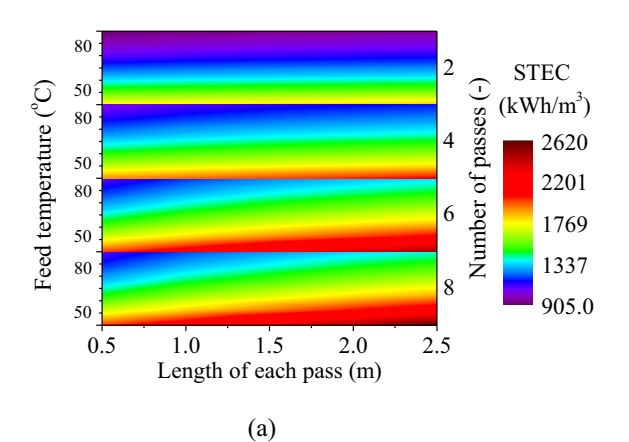
The configurations C, with the possibility of no heat recovery, and D which demonstrates the best performance in two-pass system were selected for this analysis. STEC as a function of feed temperature, length of each pass, and number of passes for the design configurations C and D have been illustrated in Fig. 4 (a) and (b), respectively. Both the figures indicate that STEC decreases by increasing the feed temperature in accordance with the literature [31,53]. At any given temperature, both configurations show similar values of STEC when the total number of passes is set equal to 2. This is due to the similar productivities and heat duties of the two configurations (Fig. A4 (a)–(d) in the Appendix) for the two-pass designs. Note that the maximum pass length (2.5 m) is half of the maximum length considered in Section 3.2, which results into relatively inefficient utilization of heat making heat recovery impossible

in the two-pass design of the configuration D because of less increase in permeate temperature. However, when the number of passes is further increased, STEC for the configuration D drops down significantly. The largest difference between the minimum STEC demonstrated by the configuration D and C is 34 %. The two configurations also exhibit opposite dependence of STEC upon number of passes and length of each pass. In configuration C, depending upon the operating temperature, STEC increases by 46–57 % with increasing the number of passes from 2 to 8 and/or by increasing the pass length from 0.5 to 2.5. STEC for the configuration D greatly decreases (maximum observed decrease is 67 %) by increasing the number of passes from 2 to 8 at a pass length of 1 m or by increasing the pass length from 0.5 to $\sim\!1.5$ m for the multipass (4–8) design configurations.

The observed trend for the two configurations (C and D) can be explained by analyzing the corresponding productivities and heat duty values provided in Fig. A4 (a)-(d). Although the productivities of both configurations are similar under any condition and shows similar response to change in the number of passes or length of each pass, yet the heat duty differs significantly, particularly at high number of passes (>2). In case of the configuration D, the heat duty does not exceed 4.5 kW in any case while it approaches to 9 kW for configuration C (Fig. A4 (c) and (d), respectively). The energy efficiency and potential of heat recovery for the design configuration D increases with increasing the feed temperature, number of passes, and length of each pass and consequently, STEC reduces. Fig. 4 (a) and (b) also demonstrate that the pass length (and hence the module length) can be significantly decreased by increasing the number of passes (or vice versa) while keeping the same STEC. For instance, in the configuration D, the pass length can be decreased to 1 m for 8 passes module which consumes the same energy as that for 2 m long module having 4 passes.

The effect of pass length and number of passes on STEC at various F/P ratios for the design configurations C and D has been shown in Fig. 5 (a) and (b), respectively. It can be noted from Fig. 5 (a) that the STEC for the configuration C at any F/P ratio increases with increasing the pass length or number of passes. Thus, the minimum STEC for the configuration C has been observed at the lowest number of passes and pass lengths for multiple pass systems which is consistent with the observations noted in Section 3.2. Like the explanation provided in the above paragraph, the observed trend follows the productivity and heat duty provided in Fig. A5 (b) and (d), respectively. With respective to C, the configuration D demonstrates opposite dependence at the number of passes and pass length i.e. at any given F/P ratio, STEC for this configuration decreases by increasing the number of passes or length of each pass. The minimum STEC for configuration D remains 34 % lower than the minimum STEC exhibited by the configuration C.

To compare the energy efficiency potential of multipass modules with the traditional single-pass module, STEC for the two designs (C and D) under the same conditions (feed inlet temperature and V_f) and pass



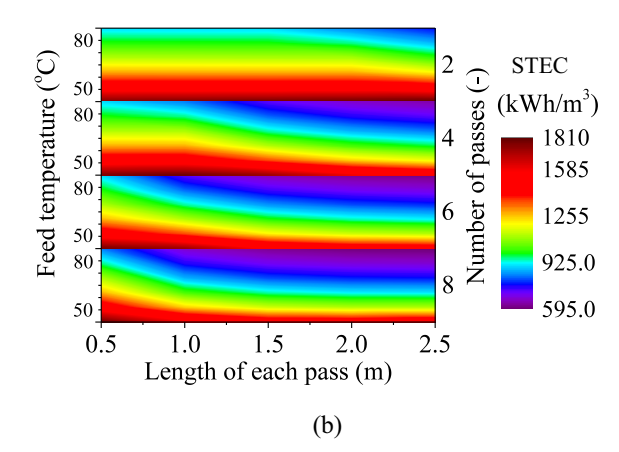


Fig. 4. STEC of (a) configuration C and (b) configuration D as a function of number of passes, length of each pass, and T_{fin} (40–90 °C).

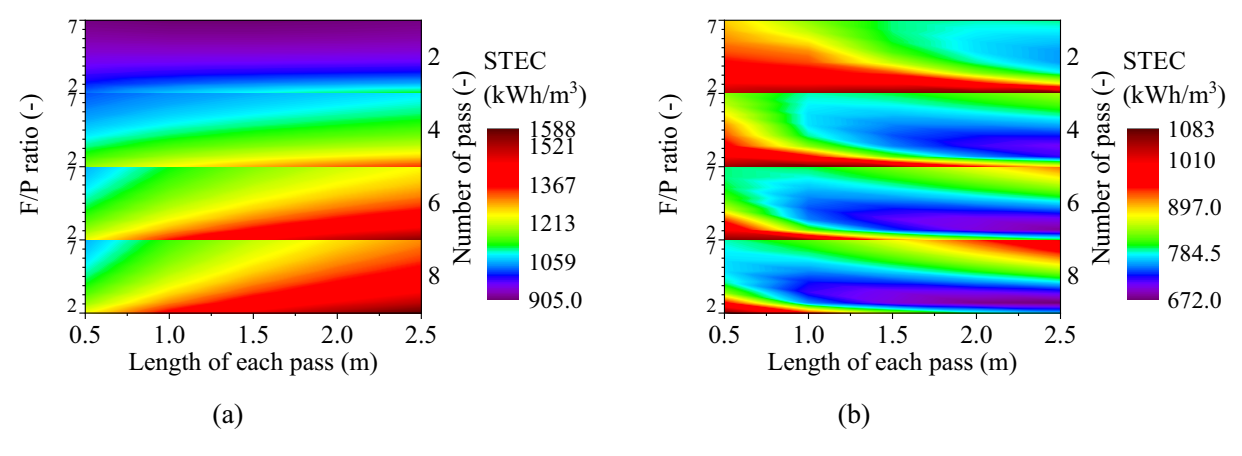


Fig. 5. STEC of (a) configuration C and (b) configuration D as function of number of passes, length of each pass and F/P ratio.

lengths can be analyzed. For this purpose, STEC of one-meter-long traditional module from our previous work [33], can be compared with the corresponding STEC of the best performing multipass design (D, Fig. 4 (b)) reported the current study. While operating at a temperature of 80 °C, one-meter-long module exhibited STEC of 970 kWh/m³ [33]. A look at Fig. 4 (b) shows that STEC of the design configuration D with respect to the traditional one-meter-long module considered in our previous work decreases by increasing the number of passes. For instance, when the maximum number of passes in the configuration D is two, the minimum STEC is around 948 kWh/m³. The difference of the minimum STEC for the two configurations further increases by 35 % with increasing the number of passes to 8 in configuration D. These observations demonstrate better energy saving potential of the multipass configurations compared to the traditional single pass configuration.

3.4. Pressure drop in the multipass modules

The pressure drop for the highest overall fiber lengths considered (20 m, Fig. 5) in the current study as function of number of passes has been shown in Fig. 6. It is evident from the figure that the pressure drop increases slightly (<100 Pa) by increasing the number of passes from 0 to 16. The figure also demonstrates that the major contribution to the overall pressure drop comes from the pressure drop within the fiber (see pressure drop corresponding to the No. of passes 0 in the figure). It is also evident from the data reported in the figure that, at the considered

average velocity (0.1 m/s), the pressure drop within the module remains significantly lower than the liquid entry pressure of the membrane (1.4 bar) used in the current study. By assuming a 50 % packing fraction, the pressure drop on the shell side remained below 50 Pa which is significantly lower than the tube side. Compared to the traditional single pass geometries, pressure drop associated with the reversal of flow direction (return loss) is the only additional pressure drop that the proposed multipass geometries suffer from. The value of the return loss remains $<\!1.5$ % of the total pressure drop even for the modules with 16 number of passes which clearly demonstrates that additional electric energy consumption of multipass modules increases only marginally compared to the conventional single pass modules.

4. Conclusions

Novel hollow fiber membrane module designs with multiple shell and fiber passes for DCMD have been proposed. The modules are particularly attractive for MD applications where the optimum fiber length appears to be several meters and the pressure losses associated with bends are not significant. It was observed that flux for the conventional one pass countercurrent design (A) was almost double compared to the multiple shell and tube pass design (D) operating in the pure countercurrent mode. However, despite yielding the lowest flux, D design has the potential to reduce up to 34 % thermal energy compared to the conventional single-pass design. Flux for single shell and multiple tube passes designs (B and C) remains somewhere between A and D

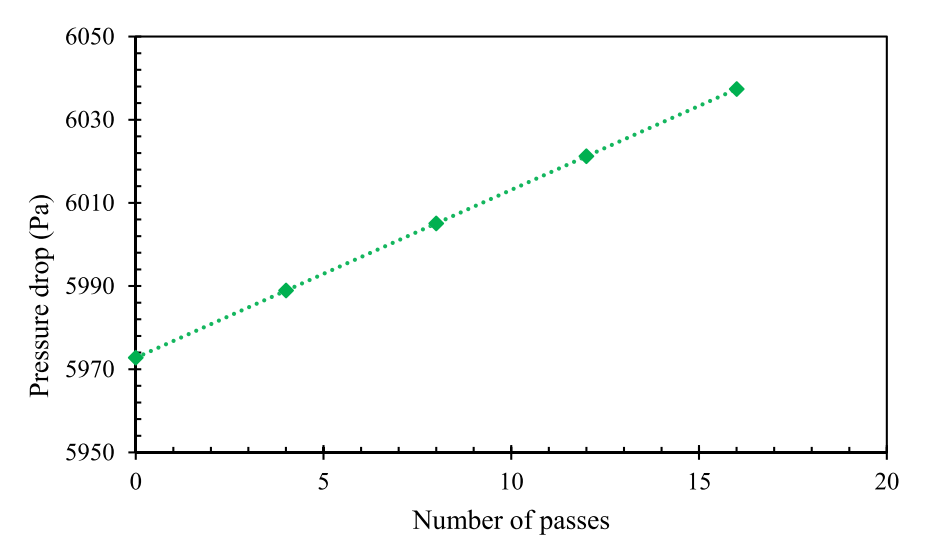


Fig. 6. Pressure drop as function of number of passes in a module with effective fiber length of 20 m.

design configurations but their energy consumptions was even higher (up to 20 %) than conventional single pass design. Due to their potential of accommodating long fiber lengths and therefore more membrane area, the multipass module exhibit productivity several times higher than the traditional one-pass design. The analysis also demonstrated that the pressure drop associated with the change of flow direction in the multipass modules contributed very less (<1.5 %) to the overall pressure drop within the module.

CRediT authorship contribution statement

Jheng-Han Tsai: Methodology, Conceptualization, Software, Formal analysis. **Cejna Quist-Jensen:** Writing – review & editing, Supervision, Funding acquisition. **Aamer Ali:** Conceptualization, Methodology, Validation, Writing – review & editing, Supervision.

Appendix

Model validation

(i) Experimentation

Declaration of competing interest

The authors declare that they have no known competing financial interests or personal relationships that could have appeared to influence the work reported in this paper.

Data availability

No data was used for the research described in the article.

Acknowledgement

This research is funded by The Ministry of Foreign Affairs of Denmark (MFA) through Danida Fellowship Centre (DFC) project no. 20-M01AAU ("Membrane crystallization for water and mineral recovery").

To generate the experimental data for the single pass module in counter and cocurrent configurations, the experiments were performed by using three different lab-made membrane modules fabricated by using commercial PP hollow fiber membranes from Membrana GmbH (membrane properties provided in Section 2.1). The modules had length of 15, 42 and 70 cm (corresponding to the membrane surface area of 0.012, 0.034, and $0.56~\rm m^2$, respectively) and were operated in conventional single pass configuration. The modules were operated at feed inlet temperatures of 38, 47 and $56~\rm c^3$ for countercurrent configurations by using pure water as feed and permeate streams. The objective was to analyze the capability of the mathematical model to predict experimental parameters (flux and outlet temperatures) for modules having different lengths. For cocurrent configuration, experimentation with these modules was carried out at $56~\rm c^3$. In all the cases, permeate temperature was fixed at $23~\pm~2$. Feed and permeate velocities were set at $0.1~\rm m/s$ for all the experiments.

MD data for the model validation were also collected by using a lab-made module having two fiber passes and a single shell pass. The feed and permeate streams were introduced inside the fiber and on shell side, respectively. The temperatures were recorded at the inlet and outlet of the feed and permeate channels as well as at the end of the 1st feed pass (mid-point, see Fig. A1 (a)). The module used in the experiment had an active membrane area of 0.013 m². The module was fabricated by using the same commercial PP hollow fiber membranes as described above. The module was tested with 1st pass in countercurrent and 2nd pass in cocurrent as well as the other way around using distillate water as feed and permeate. All the experiments were performed by using distilled water as the feed and permeate stream and feed temperature was adjusted to 45.5 ± 0.3 , 60 ± 1 , and 70 ± 1 °C for counter-current and co-current configurations. The overall objective here was to analyze the model validation for multipass modules operating under different temperatures and in different flow configurations.

In all the experiments (conventional as well as multipass modules), experimental duration was adjusted 120 to 150 min after achieving the steady state temperatures on feed and permeate sides. Flux and temperatures were recorded after every 10 min, and their average was used for the model validation. Thus, the total number of data point collected at each condition was between 12 and 15 which ensures enough repetitions to guarantee the statistical validity.

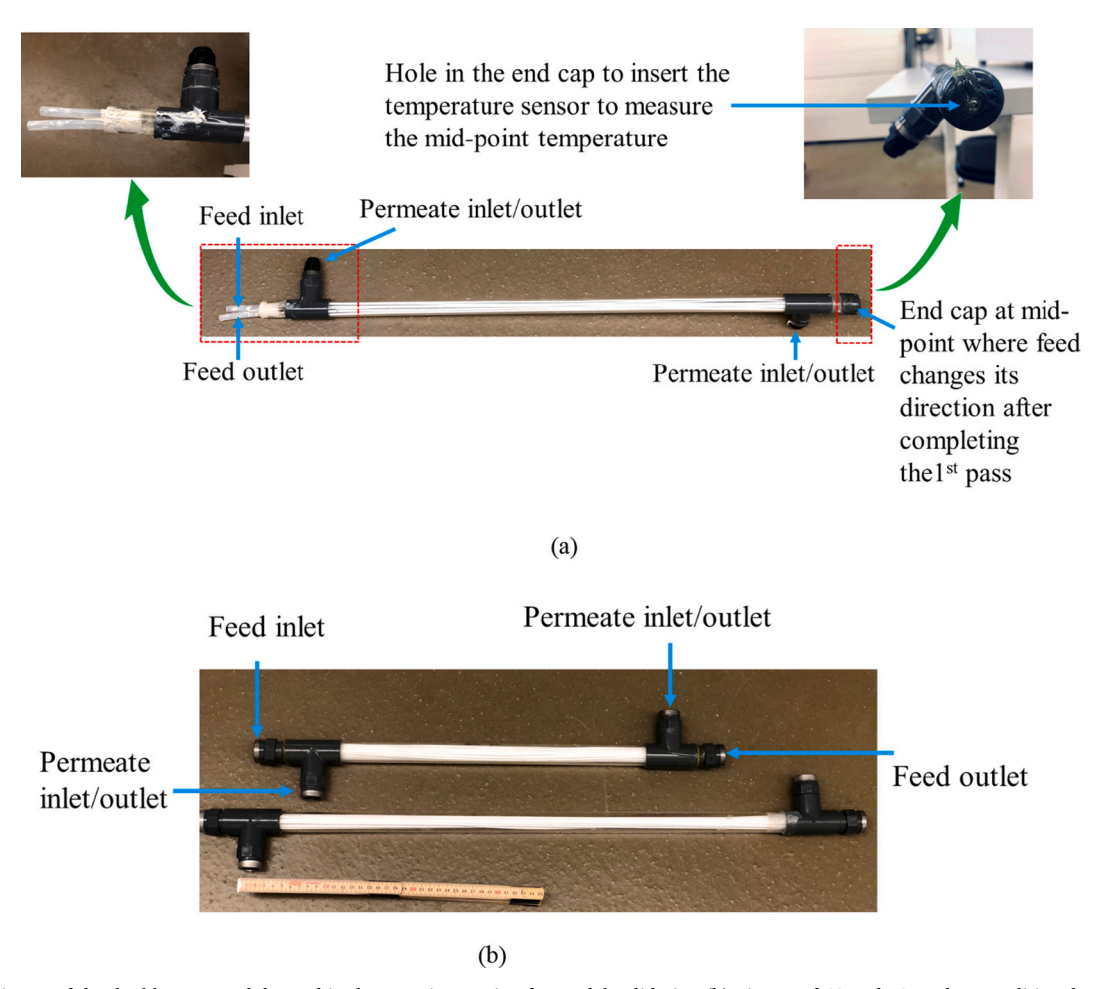
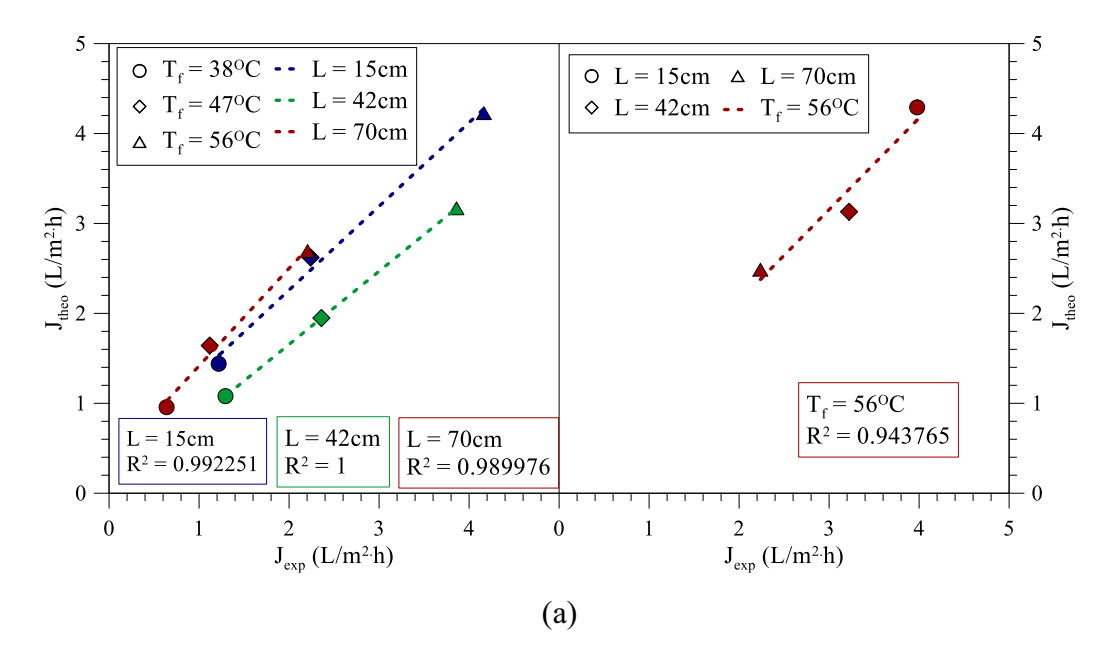


Fig. A1. (a): A picture of the double pass module used in the experimentation for model validation (b) Picture of 42 and 70 cm long traditional module used in the model validation experimentation.

(ii) Validation

The developed model was validated using different modules lengths and operating temperatures in both countercurrent and cocurrent configurations. The experimental and modeled fluxes for countercurrent and cocurrent configurations for modules with different lengths and operating under various thermal conditions have been provided in Fig. A2 (a). It is evident from the figure that for any module length, the flux increases by increasing the operating temperature. At any given temperature, the shortest (15 cm long) module exhibits the highest flux. For instance, for countercurrent configuration (Fig. A2 (a) left), the flux exhibited by 15 cm long module is \sim 55 % higher than its 70 cm long counterpart at an operating temperature of 38 °C. The difference further diverges at high feed temperatures (\sim 62 % at 56 °C operating temperature). The observed trends are consistent with the literature where a reduction in flux has been seen by increasing module length [32]. The reduction is attributed to large temperature variations along the long modules which reduces the average driving force to the mass transport. For any module length, the flux shows exponential dependence upon temperature. For instance, flux for 15 cm long module was recorded as 1.05, 1.92 and 3.1 kg/m²-h at feed inlet temperatures of 38, 47 and 56 °C, respectively. The figure also shows that the developed mathematical model can predict the experimental flux with excellent accuracy ($R^2 > 98$ %) in all the cases. As shown in Fig. A2 (a) (right), the flux exhibits the qualitative same dependence upon the module length also for cocurrent configuration and can be predicted with the sufficient accuracy by the model ($R^2 > 0.94$). The model was also used to predict the feed and permeate temperatures at outlet of the modules for countercurrent (T-coun) and cocurrent (T-co) modes and the results are illustrated in Fig. A2 (b). The figure illustrates that the model can predict the feed and permeate outlet temperatures accurately for both type of flow arrange



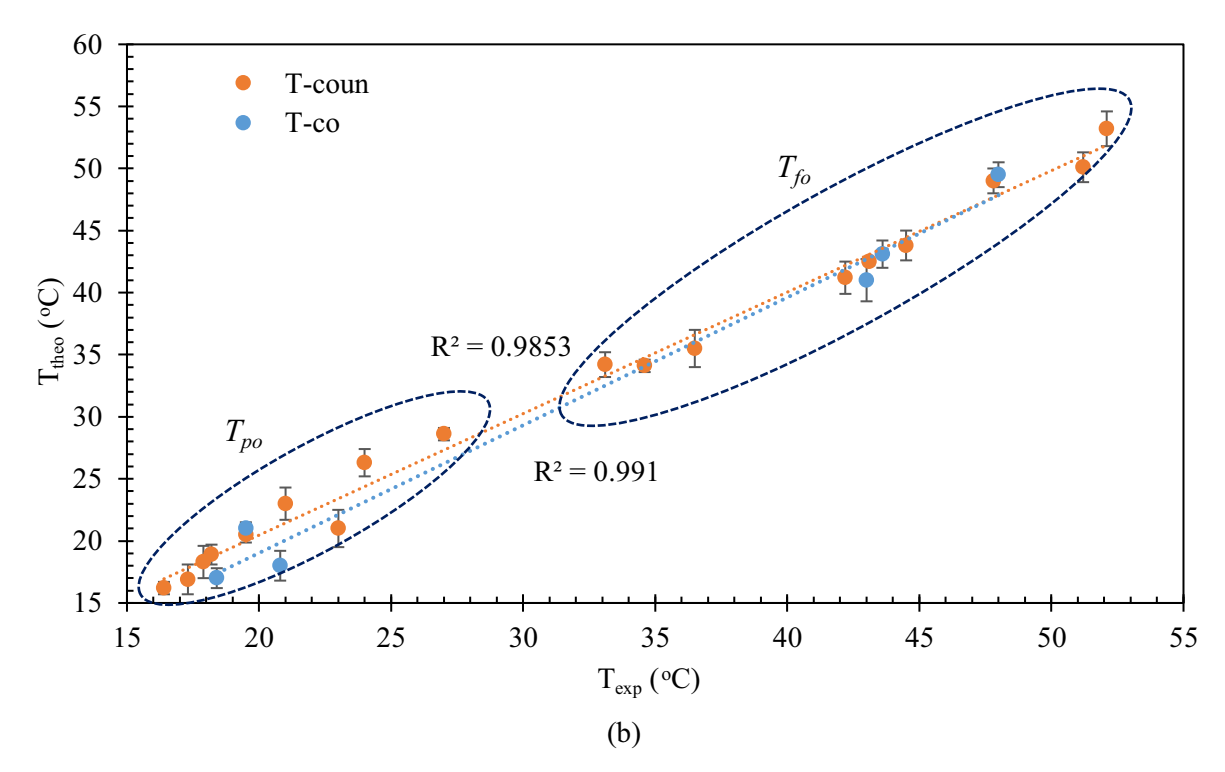
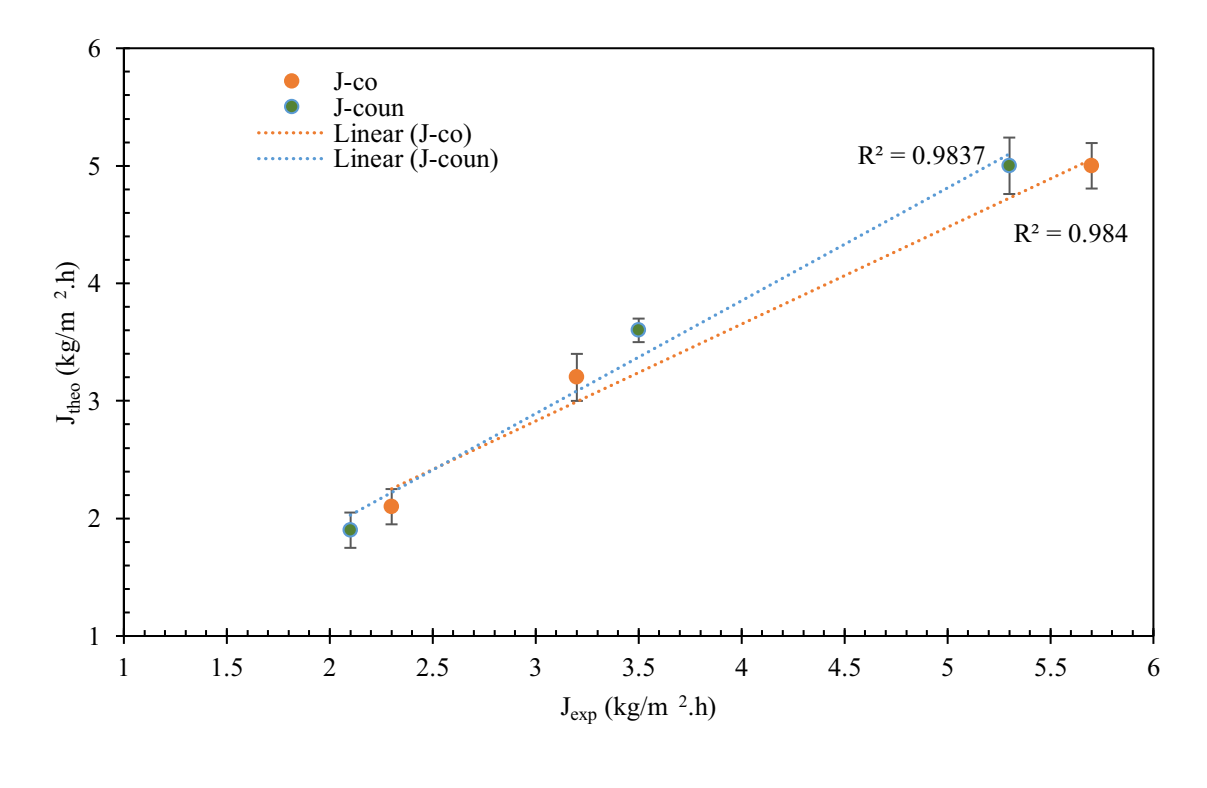


Fig. A2. Validation of developed model for single-pass module (a) experimental and theoretical flux for different modules operating in countercurrent (left) and cocurrent (right) configurations (b) experimental and modeled outlet feed and permeate temperatures for countercurrent and cocurrent modes. T_{fo} and T_{po} represent feed and permeate outlet temperatures, respectively.

The experimental and modeled data for the two fiber and one shell pass module design were also compared to check the suitability of the model for two-pass module designs operating in cocurrent and countercurrent modes. Overall experimental flux and temperatures at end of the 1st feed pass (mid) and at the exit of the feed pass have been illustrated in Fig. 3 (a) and (b), respectively. Like the single pass module, the flux increase with feed inlet temperature and difference in flux between the two operating mode is of the order of experimental error. As expected, for any feed inlet temperature, the mid-point temperature is greater than the feed outlet temperature. The figures show that the model can accurately predict the flux as well as temperatures for the two-pass design configuration operating under countercurrent as well as cocurrent mode.



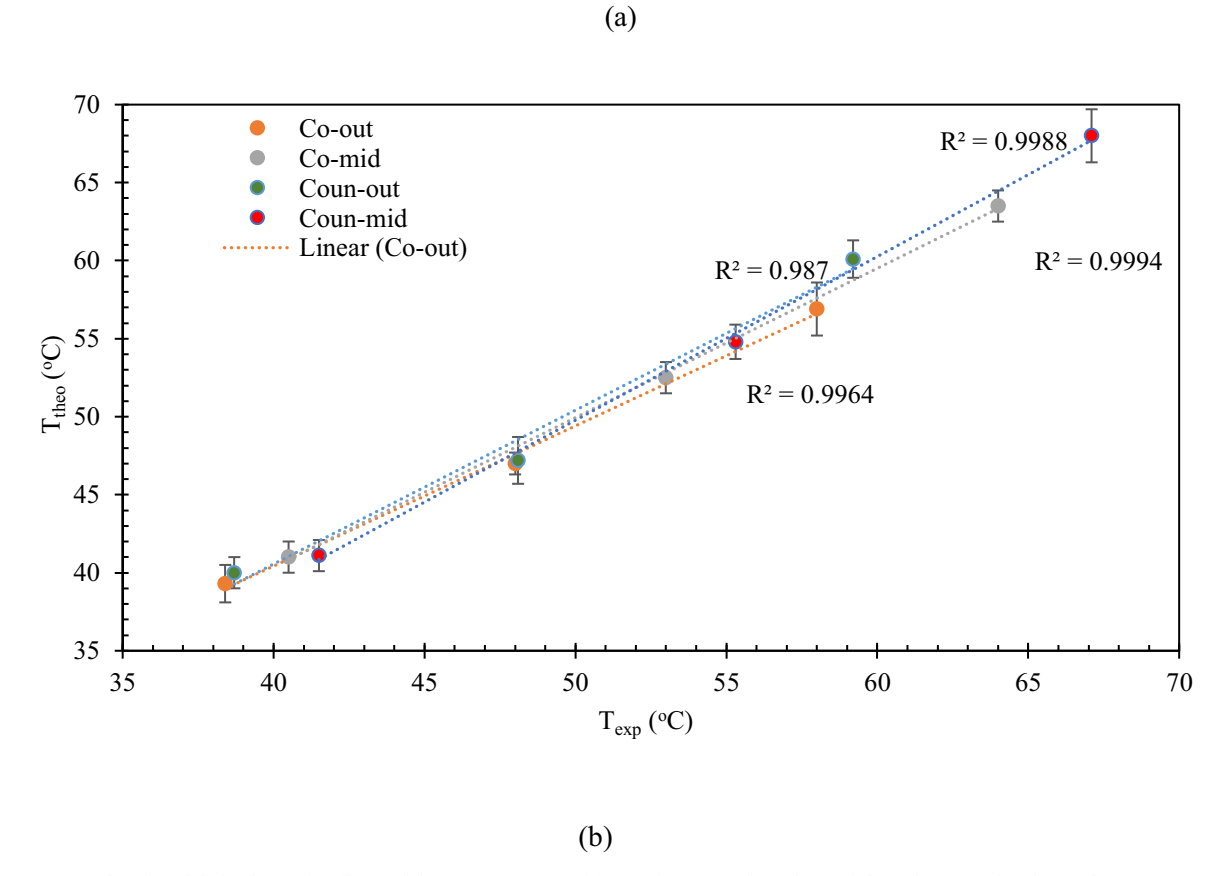


Fig. A3. Experimental and modeled values of (a) flux and (b) temperatures at different locations along the module with two feed and a single permeate pass operated in cocurrent (Co) and countercurrent (Coun) configurations.

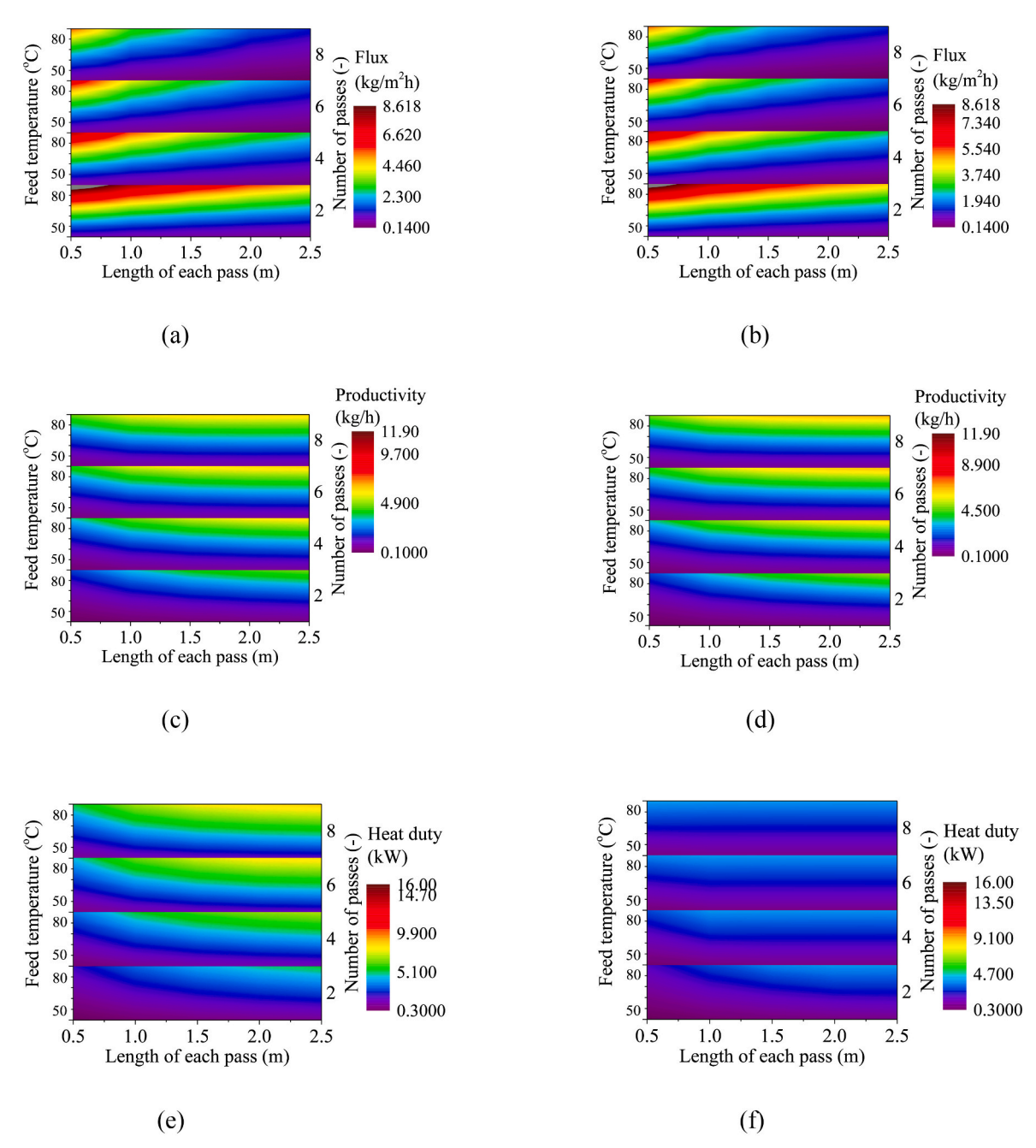


Fig. A4. Flux, productivity and heat duty for configuration C (a, c, e) and D (b, d, f) at different feed inlet temperatures.

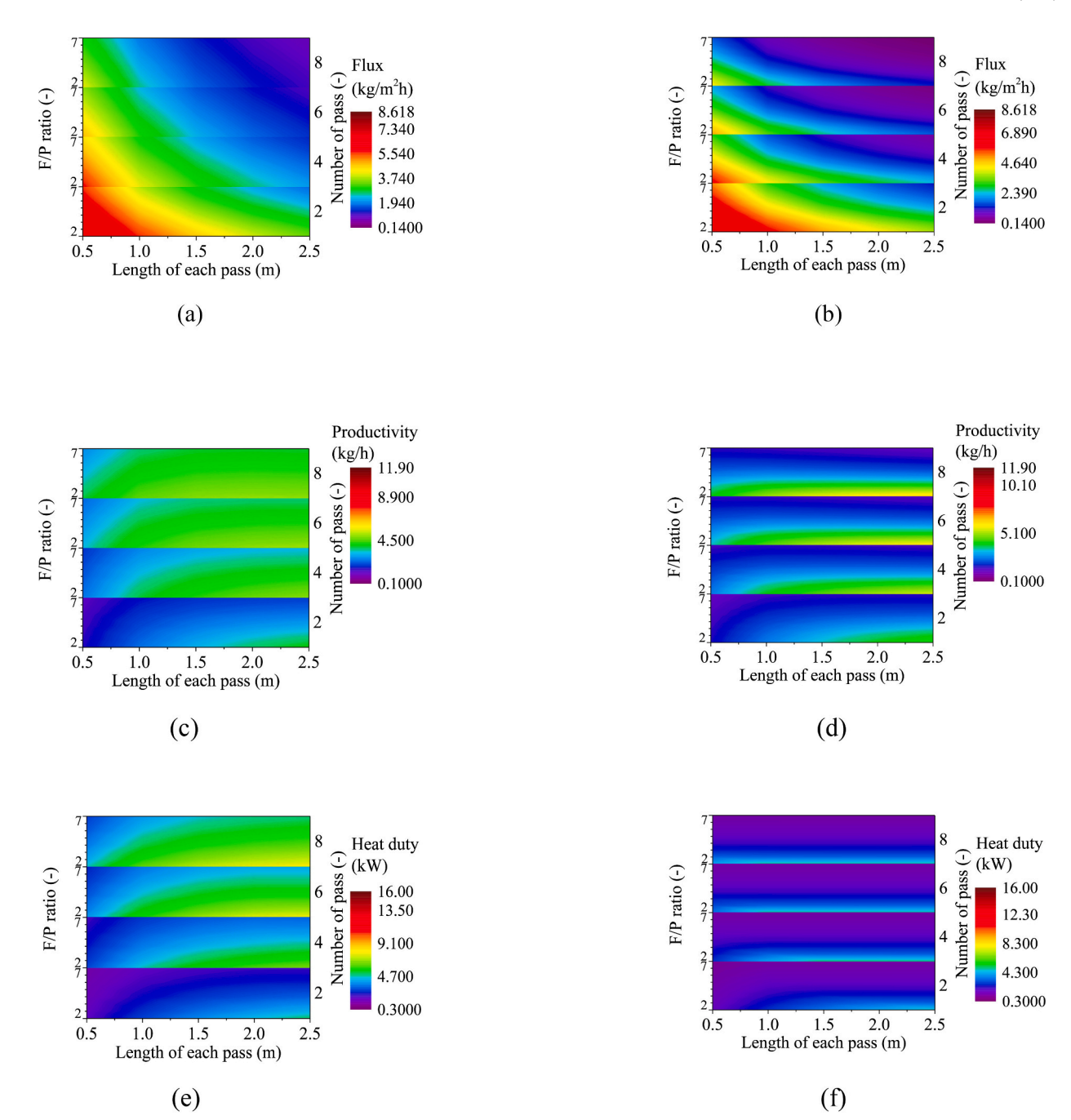


Fig. A5. Flux, productivity and heat duty as function of pass, number of passes and F/P ratio for configuration C and D.

References

- P. Wang, T. Chung, Recent advances in membrane distillation processes: membrane development, configuration design and application exploring,
 J. Membr. Sci. 474 (2015) 39–56, https://doi.org/10.1016/j.memsci.2014.09.016.
- [2] L.D. Tijing, J.-S. Choi, S. Lee, S.-H. Kim, H.K. Shon, Recent progress of membrane distillation using electrospun nanofibrous membrane, J. Membr. Sci. 453 (Mar. 2014) 435–462, https://doi.org/10.1016/j.memsci.2013.11.022.
- [3] M. Khayet, Membranes and theoretical modeling of membrane distillation: a review, Adv. Colloid Interface Sci. 164 (1–2) (May 2011) 56–88, https://doi.org/ 10.1016/j.cis.2010.09.005.
- [4] Q. Zhang, et al., Ethanol production by modified polyvinyl alcohol-immobilized Zymomonas mobilis and in situ membrane distillation under very high gravity condition, Appl. Energy 202 (2017) 1–5, https://doi.org/10.1016/j. apenergy.2017.05.105.
- [5] G. Zuo, G. Guan, R. Wang, Numerical modeling and optimization of vacuum membrane distillation module for low-cost water production, Desalination 339 (Apr. 2014) 1–9, https://doi.org/10.1016/j.desal.2014.02.005.
- [6] A. Ali, F. Macedonio, E. Drioli, S. Aljlil, O.A. Alharbi, Experimental and theoretical evaluation of temperature polarization phenomenon in direct contact membrane distillation, Chem. Eng. Res. Des. 91 (10) (Oct. 2013) 1966–1977, https://doi.org/ 10.1016/j.cherd.2013.06.030.
- [7] A. Ali, P. Aimar, E. Drioli, Effect of module design and flow patterns on performance of membrane distillation process, Chem. Eng. J. 277 (2015) 368–377, https://doi.org/10.1016/j.cej.2015.04.108.
- [8] I. Hitsov, L. Eykens, K. De Sitter, C. Dotremont, L. Pinoy, B. Van Der Bruggen, Calibration and analysis of a direct contact membrane distillation model using Monte Carlo filtering, J. Membr. Sci. 515 (2016) 63–78, https://doi.org/10.1016/j. memsci.2016.05.041.
- [9] Q. Li, et al., The potential of hollow fiber vacuum multi-effect membrane distillation for brine treatment, Appl. Energy 276 (Oct. 2020), https://doi.org/ 10.1016/j.apenergy.2020.115437.

- [10] E. Drioli, A. Ali, F. Macedonio, Membrane distillation: recent developments and perspectives, Desalination 356 (2015) 56–84, https://doi.org/10.1016/j. desal.2014.10.028.
- [11] M.M.A. Shirazi, A. Kargari, A review on applications of membrane distillation (MD) process for wastewater treatment, J. Membr. Sci. Res. 1 (2015) 101–112.
- [12] Z. Ding, L. Liu, Z. Li, R. Ma, Z. Yang, Experimental study of ammonia removal from water by membrane distillation (MD): the comparison of three configurations, J. Membr. Sci. 286 (1–2) (Dec. 2006) 93–103, https://doi.org/10.1016/j. memsci.2006.09.015.
- [13] I.B. Elkina, A.B. Gilman, V.V. Ugrozov, V.V. Volkov, Separation of Mineral Acid Solutions by Membrane Distillation and Thermopervaporation through Porous and Nonporous Membranes, 2013.
- [14] K. Zhao, et al., Experimental study of the memsys vacuum-multi-effect-membrane-distillation (V-MEMD) module, Desalination 323 (2013) 150–160, https://doi.org/10.1016/j.desal.2012.12.003.
- [15] C.-C. Ko, et al., Increasing the performance of vacuum membrane distillation using micro-structured hydrophobic aluminum hollow fiber membranes, Appl. Sci. 7 (4) (2017) 357, https://doi.org/10.3390/app7040357.
- [16] H. Lee, F. He, L. Stone, J. Gilron, K.K. Sirkar, Desalination with a cascade of cross-flow hollow fiber membrane distillation devices integrated with a heat exchanger, AIChE J. 57 (7) (2011) 1780–1795
- [17] H. Geng, H. Wu, P. Li, Q. He, Study on a new air-gap membrane distillation module for desalination, Desalination 334 (1) (Feb. 2014) 29–38, https://doi.org/ 10.1016/j.desal.2013.11.037.
- [18] F. He, J. Gilron, K.K. Sirkar, High water recovery in direct contact membrane distillation using a series of cascades, Desalination 323 (Aug. 2013) 48–54, https://doi.org/10.1016/j.desal.2012.08.006.
- [19] A.E. Sanchez, N. Goel, T. Otanicar, Novel hybrid solar nanophotonic distillation membrane with photovoltaic module for co-production of electricity and water, Appl. Energy 305 (Jan. 2022), https://doi.org/10.1016/j.apenergy.2021.117944
- [20] N. Peng, et al., Evolution of polymeric hollow fibers as sustainable technologies: past, present, and future, Prog. Polym. Sci. 37 (10) (2012) 1401–1424, https://doi.org/10.1016/j.progpolymsci.2012.01.001.
- [21] F. Banat, Economic and Technical Assessment of Desalination Technologies, 2007. www.desaline.com/Geneva/Banat.pdf.
- [22] A. Ali, C.A. Quist-Jensen, F. Macedonio, E. Drioli, Optimization of module length and membrane thickness for membrane distillation, in: 2nd International Workshop on Membrane Distillation and Innovating Membrane Operations in Desalination and Water Reuse, Ravello, Italy, 2016.
- [23] S. Lin, N.Y. Yip, M. Elimelech, Direct contact membrane distillation with heat recovery: thermodynamic insights from module scale modeling, J Memb Sci 453 (2014) 498–515. https://doi.org/10.1016/j.memsci.2013.11.016.
- [24] J.A. Andrés-Mañas, A. Ruiz-Aguirre, F.G. Acién, G. Zaragoza, Assessment of a pilot system for seawater desalination based on vacuum multi-effect membrane distillation with enhanced heat recovery, Desalination 443 (March) (2018) 110–121. https://doi.org/10.1016/j.desal.2018.05.025.
- [25] A. Criscuoli, Thermal performance of integrated direct contact and vacuum membrane distillation units, Energies (Basel) 14 (21) (Nov. 2021), https://doi.org/ 10.3390/en14217405.
- [26] J.A. Andrés-Mañas, A. Ruiz-Aguirre, F.G. Acién, G. Zaragoza, Performance increase of membrane distillation pilot scale modules operating in vacuum-enhanced airgap configuration, Desalination 475 (November 2019) (2020), 114202, https:// doi.org/10.1016/j.desal.2019.114202.
- [27] D. Winter, Membrane Distillation: A Thermodynamic, Technological and Economic Analysis, Shaker Verlag GmbH, 2015.
- [28] D. Winter, J. Koschikowski, M. Wieghaus, Desalination using membrane distillation: experimental studies on full scale spiral wound modules, J. Membr. Sci. 375 (1–2) (2011) 104–112, https://doi.org/10.1016/j.memsci.2011.03.030.

- [29] D. Winter, et al., Comparative analysis of full-scale membrane distillation contactors - methods and modules, J. Membr. Sci. 524 (October 2016) (2017) 758–771, https://doi.org/10.1016/j.memsci.2016.11.080.
- [30] A. Ruiz-Aguirre, J.A. Andrés-Mañas, J.M. Fernández-Sevilla, G. Zaragoza, Experimental characterization and optimization of multi-channel spiral wound air gap membrane distillation modules for seawater desalination, Sep. Purif. Technol. 205 (May) (2018) 212–222, https://doi.org/10.1016/j.seppur.2018.05.044.
- [31] A. Ali, C.A.A. Quist-Jensen, F. Macedonio, E. Drioli, Optimization of module length for continuous direct contact membrane distillation process, Chem. Eng. Process. Process Intensif. 110 (2016) 188–200, https://doi.org/10.1016/j.cep.2016.10.014.
- [32] A. Ali, C.-A.Q. Jensen, F. Macedonio, E. Drioli, On designing of membrane thickness and thermal conductivity for membrane distillation, J. Membr. Sci. Res. 2 (2016).
- [33] A. Ali, J.-H. Tsai, K.-L. Tung, E. Drioli, F. Macedonio, Designing and optimization of continuous direct contact membrane distillation process, Desalination 426 (2018) 97–107, https://doi.org/10.1016/j.desal.2017.10.041.
- [34] A. Ali, A. Criscuoli, F. Macedonio, E. Drioli, A comparative analysis of flat sheet and capillary membranes for membrane distillation applications, Desalination 456 (July 2018) (2019) 1–12, https://doi.org/10.1016/j.desal.2019.01.006.
- [35] N.C. Mat, Y. Lou, G.G. Lipscomb, Hollow fiber membrane modules, Curr. Opin. Chem. Eng. 4 (2014) 18–24, https://doi.org/10.1016/j.coche.2014.01.002.
- [36] J. Zheng, Y. Xu, Z. Xu, Flow distribution in a randomly packed hollow fiber membrane module, J. Membr. Sci. 211 (2003) 263–269.
- [38] Stephen A. Rackley, Membrane separation systems, in: Carbon Capture and Storage, 2nd ed., Butterwork-Heinemann, 2017, pp. 187–225.
- Storage, 2nd ed., Butterwork-Heinemann, 2017, pp. 187–225.
 [39] Keith Scott, Introduction to membrane separations, in: Handbook of Industrial Membranes, 1st ed., Elsevier B.V, 1995, pp. 3–185.
- [40] H.M. Yeh, J.W. Tsai, Membrane ultrafiltration in multipass hollow-fiber modules, J. Membr. Sci. 142 (1) (1998) 61–73, https://doi.org/10.1016/S0376-7388(97) 002323
- [41] A. Bejan, A.D. Kraus, Heat transfer handbook, John Wiley, 2003.
- [42] L.C. Thomas, Heat Transfer, Prentice-Hall, Englewood Cliffs, NJ, 1992.
- [43] D.O. Kern, Process Heat Transfer, Internatio, McGraw-Hill International, 1983.
- [44] J.M. Coulson, J.F. Richardson, J.R. Backhurst, J.H. Harker, Coulson and Richardson's Chemical Engineering: Fluid Flow, Heat Transfer and Mass Transfer, 6th ed., Elsevier, 1999.
- [45] C.F. Wan, T. Yang, G.G. Lipscomb, D.J. Stookey, T. Chung, Design and fabrication of hollow fiber membrane modules, J. Membr. Sci. 538 (May) (2017) 96–107, https://doi.org/10.1016/j.memsci.2017.05.047.
- [46] Y.A. Cengel, Heat exchangers, in: Heat Transfer A Practical Approach, 2nd ed., McGraw-Hill Higher Education, 2002, pp. 61–126.
- [47] L. Camacho, et al., Advances in membrane distillation for water desalination and purification applications, Water (Basel) 5 (1) (Jan. 2013) 94–196, https://doi.org/ 10.3390/w5010094.
- [48] J. Phattaranawik, R. Jiraratananon, A.G. Fane, Effect of pore size distribution and air flux on mass transport in direct contact membrane distillation, J. Membr. Sci. 215 (1–2) (Apr. 2003) 75–85, https://doi.org/10.1016/S0376-7388(02)00603-8.
- [49] S.B. Iversen, V.K. Bhatia, K. Dam-Johansen, B.G. Jonsson, Characterization of Microporous Membranes for Use in Membrane Contactors, 1997.
- [51] S. Yoshikawa, K. Ogawa, S. Minegishi, Distribution of pressure drop and flow rate in a hollow-fiber membrane module for plasma separation, Journal of Chemical Engineering of Japan 27 (3) (1994) 385–390.
- [52] J. Zhang, S. Gray, J. de Li, Predicting the influence of operating conditions on DCMD flux and thermal efficiency for incompressible and compressible membrane systems, Desalination 323 (Aug. 2013) 142–149, https://doi.org/10.1016/j. desal.2013.04.002.
- [53] A. Ali, C.A. Quist-Jensen, F. Macedonio, E. Drioli, On designing of membrane thickness and thermal conductivity for large scale membrane distillation modules, J. Membr. Sci. Res. 2 (4) (2016) pp.